bioRxiv preprint doi: https://doi.org/10.1101/2022.09.11.507445; this version posted September 11, 2022. The copyright holder for this preprint (which was not certified by peer review) is the author/funder, who has granted bioRxiv a license to display the preprint in perpetuity. It is made available under aCC-BY-NC 4.0 International license.

For Method articles

Title

An ImageJ-based tool for three-dimensional registration between different types of microscopic images

Authors

Hiroshi Koyama[1,2,*], Kanae Kishi[1,3], and Toshihiko Fujimori[1,2,3]

[1]Division of Embryology, National Institute for Basic Biology, 5-1 Higashiyama, Myodaiji, Okazaki, Aichi 444-8787, Japan

[2]SOKENDAI (The Graduate University for Advanced Studies), Hayama, Kanagawa 240-0193, Japan

[3]Japan Science and Technology Agency, Core Research for Evolutional Science and Technology (JST-CREST), Kawaguchi, Saitama, Japan 3

*Correspondence: Hiroshi Koyama

bioRxiv preprint doi: https://doi.org/10.1101/2022.09.11.507445; this version posted September 11, 2022. The copyright holder for this preprint (which was not certified by peer review) is the author/funder, who has granted bioRxiv a license to display the preprint in perpetuity. It is made available under aCC-BY-NC 4.0 International license.

19 Division of Embryology, National Institute for Basic Biology, 5-1

20 Higashiyama, Myodaiji, Okazaki, Aichi 444-8787, Japan

21 Phone: +81 564 59 5862,

22 hkoyama@nibb.ac.jp.

23

24 Conflicts of interest

25 The authors declare no competing financial interests.

26

27 Keywords

28 Image registration, three-dimensional image rotation, mouse early embryo, ImageJ

29

30

bioRxiv preprint doi: https://doi.org/10.1101/2022.09.11.507445; this version posted September 11, 2022. The copyright holder for this preprint (which was not certified by peer review) is the author/funder, who has granted bioRxiv a license to display the preprint in perpetuity. It is made available under aCC-BY-NC 4.0 International license.

Abstract

Three-dimensional (3D) registration (i.e. alignment) between two microscopic images is substantially helpful to study tissues not adhere to substrates such as mouse embryos and organoids which are often three-dimensionally rotated during imaging. However, there is no 3D registration tool easily accessible for experimental biologists. Here we developed an ImageJ-based tool which achieves 3D registration accompanying both quantitative evaluation of the accuracy and reconstruction of 3D rotated images. In this tool, several landmarks are manually provided in two images to be aligned, and 3D rotation is computed so that the distances between the paired landmarks from the two images are minimized. By simultaneously providing multiple points (e.g. all nuclei in the regions of interest) other than the landmarks in the two images, the correspondence of each point between the two images is quantitatively explored: a certain nucleus in one image corresponds to which nucleus in another image. Furthermore, the 3D rotation is applied to one of the two images, resulting in reconstruction of 3D rotated images. We demonstrated that this tool successfully achieved 3D registration and reconstruction of images in mouse pre-implantation embryos, where one image was obtained during live imaging and another image from fixed embryos after live imaging. This approach provides a versatile tool applicable for various tissues and species.

bioRxiv preprint doi: https://doi.org/10.1101/2022.09.11.507445; this version posted September 11, 2022. The copyright holder for this preprint (which was not certified by peer review) is the author/funder, who has granted bioRxiv a license to display the preprint in perpetuity. It is made available under aCC-BY-NC 4.0 International license.

bioRxiv preprint doi: https://doi.org/10.1101/2022.09.11.507445; this version posted September 11, 2022. The copyright holder for this preprint (which was not certified by peer review) is the author/funder, who has granted bioRxiv a license to display the preprint in perpetuity. It is made available under aCC-BY-NC 4.0 International license.

Introduction

Three-dimensional (3D) imaging is a central technique in developmental biology and organoid studies, which is achieved by confocal microscopies, multiphoton microscopies, micro-CT (computed tomography), etc. During live imaging of tissues such as early embryos of mice, chordates, and echinoderms, and organoids, they can be three-dimensionally rotated in the cultured medium/liquid because they do not adhere to substrates. In studies relating to cell tracking and cell lineage, researchers have to pay much efforts to determine the correspondence of each cell between images before and after the rotation (Koyama et al., 2022; Kurotaki et al., 2007). Similar issues also raise when researchers compare live imaging data with images obtained from samples fixed after live imaging (Fig. 1) (Pokrass et al., 2020; Simon et al., 2020); e.g. characteristics different from those obtained from the live imaging are visualized from fixed samples that are subjected to immunostaining, while the tissues are rotated during fixation. In addition, alignment between different embryos at a similar embryonic stage is also helpful for comparing differences of cell lineage and positions between the different embryos (Onuma et al., 2020). Under these situations, researchers physically correct the rotations during sample preparations on microscopic stages or correct on the basis of manual image processing (Onuma et al., 2020; Pokrass and Regot, 2021; Simon et al., 2020), both of

bioRxiv preprint doi: https://doi.org/10.1101/2022.09.11.507445; this version posted September 11, 2022. The copyright holder for this preprint (which was not certified by peer review) is the author/funder, who has granted bioRxiv a license to display the preprint in perpetuity. It is made available under aCC-BY-NC 4.0 International license.

71 which are usually time-consuming processes. In the former case, an exact correction is
72 almost impossible (i.e. spatial discrepancies between two images remain to some extent),
73 which may be problematic for spatially intricate regions in tissues. In the latter case, the
74 correspondence of each cell between two images is performed without reconstructing
75 three-dimensionally rotated images, and thus the outcomes of the operations are not
76 clearly presented. Therefore, it is difficult for other researchers (and even for the
77 researchers doing the manual operations) to evaluate whether the corrections are reliable.
78 To improve these situations, it is critical to develop an image processing tool for 3D
79 registration accompanying both visualization and quantitative evaluation of the outcomes,
80 which should be easily accessible for experimental biologists who are not so familiar to
81 image processing.

82 For experimental biologists, the ImageJ software and its high-functionality
83 version Fiji are the most widely accessible image processing tools. In default plugins
84 implemented in Fiji, “Correct 3D drift” is a 3D registration tool, but it only considers 3D
85 translation (i.e. x, y, and z-directional movements) but not rotation. Another 3D
86 registration plugin called “Descriptor-based registration (2d/3d)” is implemented for
87 specific situations where many beads are embedded as landmarks in samples and are
88 computationally detected for subsequent usage of 3D registration (Preibisch et al., 2010).

bioRxiv preprint doi: https://doi.org/10.1101/2022.09.11.507445; this version posted September 11, 2022. The copyright holder for this preprint (which was not certified by peer review) is the author/funder, who has granted bioRxiv a license to display the preprint in perpetuity. It is made available under aCC-BY-NC 4.0 International license.

A more primitive way is manual operations of "Rotate" and "Reslice" tools, both of which are basic functions in ImageJ/Fiji; through multiple cycles of these two tools, any 3D rotation and subsequent 3D reconstruction can in principle be achieved. However, as far as we tried, it is very hard to determine correct 3D rotations and angles of reslices, probably except for researchers who can easily imagine 3D rotation of objects. Image processing tools other than ImageJ have been developed for experimental biology especially for segmentation of two-dimensional epithelial cells and subsequent quantitative analyses (Heller et al., 2016; Tan et al., 2021), and for segmentation of objects in three-dimensional tissues (Azuma and Onami, 2017; Bao et al., 2006; McDole et al., 2018).

In the present study, we developed a versatile 3D registration/rotation tool which can be applicable for any types of 3D images and can be run on ImageJ.

Materials and Methods

Mouse embryos

The mouse embryos at the blastocyst stage were used as the test case. We performed confocal fluorescent microscopic imaging of fluorescently-labeled nuclei in living

bioRxiv preprint doi: https://doi.org/10.1101/2022.09.11.507445; this version posted September 11, 2022. The copyright holder for this preprint (which was not certified by peer review) is the author/funder, who has granted bioRxiv a license to display the preprint in perpetuity. It is made available under aCC-BY-NC 4.0 International license.

107 embryos in a manner similar to our previous works (Fig. 2, 1st image) (Azuma and Onami,
108 2017; Koyama et al., 2022). Subsequently, we fixed the embryos, stained the nuclei by
109 Hoechst, and then imaged them (Fig. 2, 2nd image). The blastocysts are composed of two
110 cell types: the trophectoderm (TE) cells form an outermost layer and the inner cell mass
111 (ICM) cells form an inner cell aggregate with high cell density (Fig. 2, illustration). The
112 image obtained from the fixed embryos showed rotation compared with the image from
113 living embryos (Fig. 2; see the location of ICMs).

114 The microscopic imaging conditions are as follows: the confocal microscopy
115 (A1 laser scanning confocal microscope, Nikon, Japan) with a 60× objective (PlanApo;
116 WI; NA=1.20, Nikon, Japan), Z-slices separated by 0.575μm for live embryos or
117 0.625μm for fixed embryos. The nuclei in the live or fixed embryos were labeled by YFP
118 conjugated with a nuclear localization signal or Hoechst, respectively.

119

120 *Overview of methods for 3D-registration*

121 For studies of cell lineage in the mouse early embryos (Kurotaki et al., 2007; Pokrass et
122 al., 2020; Simon et al., 2020), 3D registration during live imaging or between live and
123 fixed embryos substantially supports the analyses. We developed a landmark-based 3D
124 registration and applied to the blastocysts. The overview of our method is illustrated in

bioRxiv preprint doi: https://doi.org/10.1101/2022.09.11.507445; this version posted September 11, 2022. The copyright holder for this preprint (which was not certified by peer review) is the author/funder, who has granted bioRxiv a license to display the preprint in perpetuity. It is made available under aCC-BY-NC 4.0 International license.

Fig. 3. In the first step, as landmarks, we manually chose several pairs of the same nuclei between the 1st and 2nd images (Fig. 3A, step-1). In addition to the landmarks, we manually chose all objects (i.e. nuclei) of interest in the both images, which are not paired at this moment (Fig.3A, step-2). The manual steps needed in our method are limited to the above two steps, and thus, user's effort is minimum. The next step is the core in our method, where 3D rotation was computationally performed so that the summation of the distances between the paired landmarks became minimized (Fig. 3A, step-4). Note that this summation is called the cost function to be minimized. In the present case, the landmarks in the 2nd image were rotated. In general, 3D rotation is expressed as a matrix composed of three rotational angles (Fig. 3B), while 2D rotation is of one rotational angle (Fig. 3B). Therefore, the optimal values of these three angles were computed; the mathematical algorithm is explained in Appendix.

By using the optimal values of the three angles, we performed following two analyses. 1) The xyz-coordinates of the nuclei of interest chosen in the previous step were computationally rotated according to the three rotational angles (Fig. 3A, step-5). For each nucleus in the live embryos, we computationally determined the nearest nucleus in the fixed embryos. In other words, we determined the correspondences of the several tens of the nuclei between the live and fixed embryos (Fig. 3A, step-5, "pairs"). 2) We also

bioRxiv preprint doi: https://doi.org/10.1101/2022.09.11.507445; this version posted September 11, 2022. The copyright holder for this preprint (which was not certified by peer review) is the author/funder, who has granted bioRxiv a license to display the preprint in perpetuity. It is made available under aCC-BY-NC 4.0 International license.

143 applied the rotation based on the three rotational angles to the images from the fixed
144 embryos, and reconstructed 3D images (Fig. 3A, step-6). Consequently, we can easily
145 compare the resultant 3D images with the images from the live embryos. These two
146 analyses enabled us to quantitatively and visually determine the correspondences of the
147 nuclei between the live and fixed embryos.

148 In addition to the above steps, we implemented optional steps to adjust real
149 situations. In real tissues, fixation often shrink tissues. Moreover, conditions of
150 microscopic imaging cause shrinkage or elongation of 3D images along the Z-axis; e.g.
151 differences of refractive indices between glass of the glass-base dishes and medium for
152 specimen. Severe shrinkage or elongation can spoil the 3D registration. We can revise the
153 x, y, and z scales in both the live and fixed embryos before or after the choice of the
154 landmarks (Fig. 3A, "[Optional…" and step-3).

155

156 Results

157 *3D rotation of landmarks and objects of interest*

158 We applied our method to the mouse blastocysts. In Fig. 2 ("Z-slice" and "MIP"), we
159 chose 9 nuclei as landmarks. In addition to the landmarks, we also labeled several tens of
160 the nuclei as objects of interest. We loaded the xyz-coordinates of the landmarks into our

bioRxiv preprint doi: https://doi.org/10.1101/2022.09.11.507445; this version posted September 11, 2022. The copyright holder for this preprint (which was not certified by peer review) is the author/funder, who has granted bioRxiv a license to display the preprint in perpetuity. It is made available under aCC-BY-NC 4.0 International license.

ImageJ-macro, and then, computationally obtained the values of the three angles for 3D rotation. Note that the rotation centers in the two images were set at the centroids of the landmarks. Finally, we generated an image where the rotated positions of the landmarks were depicted as particles. This image is a 3D image (i.e. composed of multiple z-slices) Fig 4A shows a merged 3D image of the landmarks from the 1st and 2nd images. Before the rotation, the landmarks from the two images were not closely located (Fig. 4A, left panel), whereas, after the rotations, the landmarks became closely located (Fig. 4A, right panel).

Then, we applied the 3D rotation to the positions of the nuclei other than the landmarks, and generated a 3D image (i.e. composed of multiple z-slices). In the 3D image where the nuclei from the 1st and the rotated 2nd images were merged (Fig. 4B, left panel), most of the nuclei from the two images were closely located and paired each other (e.g. labeled by yellow). We can also find several nuclei which did not have counterparts (e.g. labeled by light blue with dashed line), this is because we failed to label all the nuclei at the step-2 in Fig. 3. In other words, the 3D visualization helped us to judge whether we successfully label all nuclei of interest. In addition, we can also check the localization of the positions of the rotated nuclei in each Z-slice (Fig. 4B, right panel).

To determine the correspondence of each nucleus between the 1st and the rotated

bioRxiv preprint doi: https://doi.org/10.1101/2022.09.11.507445; this version posted September 11, 2022. The copyright holder for this preprint (which was not certified by peer review) is the author/funder, who has granted bioRxiv a license to display the preprint in perpetuity. It is made available under aCC-BY-NC 4.0 International license.

179 2nd images, we calculated the distances between the nuclei in the two images. For each
180 nucleus in the 1st image, we searched for the nearest nucleus in the rotated 2nd image. Fig.
181 4C show the ID of the nearest nucleus and the distance between the paired nuclei. We
182 also searched for the 2nd and 3rd nearest nuclei as shown in Fig. 4C. By quantitatively
183 evaluating the distances of these three candidates, we can judge which nucleus is the
184 counterpart of each nucleus from the 1st image. Simultaneously, under an assumption that
185 the nearest nucleus is the correct counterparts, we generated a 3D image where the paired
186 nuclei were presented by the same color (Fig. 4D).
187
188 *3D reconstruction of rotated image*
189 We developed an algorithm to reconstruct rotated 2nd images. We applied the above 3D
190 rotation to the 2nd image itself (i.e. pixel/voxel-based rotation is applied). In Fig. 5A, the
191 rotated 2nd image is shown (blastocyst #1 vs. Fig. 2 which are the images before the
192 rotation). A merged image of the 1st and the rotated 2nd images exhibited good
193 correspondences of the nuclei. Moreover, the correspondences are also confirmed by
194 visualizing Z-slice images in Fig. 5B (e.g. labeled by yellow). The slight spatial
195 discrepancies between some pairs of the nuclei may result from shrinkage of the
196 blastocyst by the fixation. Chromosome segregation was observed in the 2nd image (Fig.

bioRxiv preprint doi: https://doi.org/10.1101/2022.09.11.507445; this version posted September 11, 2022. The copyright holder for this preprint (which was not certified by peer review) is the author/funder, who has granted bioRxiv a license to display the preprint in perpetuity. It is made available under aCC-BY-NC 4.0 International license.

5B, at the upper right of Z-slice #2, which was stained by Hoechst), whereas the signal in the 1st image was obscure; this is because the nuclear localization signal which does not bind to the chromosomes was used in the 1st image. Another example of the blastocyst is shown in Fig. 5A (blastocyst #2). Although the directions between the 1st and the 2nd image before the rotation were quite different (1st image vs. before rotation), the directions became absolutely aligned after the rotation (1st image vs. rotated 2nd image), and the merged image showed clear correspondences between the paired nuclei.

As an additional function in our tool, we can generate merged images between the nuclear images and the particle images (Fig. 5C), which is useful to identify the IDs of the nuclei in the nuclear images.

Performance and accuracy of our algorithm

We evaluated the performance of our algorithm. In our method, we searched for the optimal values of the three rotation angles as described previously. This kind of problem is called a minimization problem. In general, a minimization problem has a risk that the outcome is trapped at local minima of the cost function to be minimized but not the global minimum which provides the optimal values. In our case, the cost function is the summation of distances between the paired landmarks as defined in Materials & Methods.

bioRxiv preprint doi: https://doi.org/10.1101/2022.09.11.507445; this version posted September 11, 2022. The copyright holder for this preprint (which was not certified by peer review) is the author/funder, who has granted bioRxiv a license to display the preprint in perpetuity. It is made available under aCC-BY-NC 4.0 International license.

To reduce the risk, we performed multiple sets of minimizations in parallel from different initial values of the three rotation angles. For each angle, we set three initial values, resulting in 27 ($3 \times 3 \times 3$) sets of minimization processes running (Fig. 6A, vertical axis, "27 trials"). Some sets may reach at the global minimum, while other sets may be trapped at local minima. In Fig. 6A, we calculated the probability of reaching the global minimum (i.e. the numbers of the trials reaching the global minimum among the 27 trials). In the case of landmarks = 9, three blastocysts showed high probabilities (#2,3,4), whereas one blastocyst showed low probability (#1). Among the 9 landmarks, we randomly selected 3, 5, or 7 landmarks, and performed the minimizations. For each blastocyst, the number of the landmarks did not significantly affect the probability. These results suggest that the probability is largely dependent on individual blastocysts but not the numbers of landmarks.

Next, we evaluated the accuracy of pairing the nuclei other than the landmarks. We manually defined the correct pairs of the nuclei, and examined whether the outcomes of the minimization are consistent with the correct pairs. Note that we only considered the outcomes of the global minimum. Fig. 6B shows the percentage of the correct pairs of the nuclei. In the case of landmarks = 9, all pairs obtained by the minimization were correct (i.e. accuracy = 100%). On the other hand, under smaller numbers of landmarks

bioRxiv preprint doi: https://doi.org/10.1101/2022.09.11.507445; this version posted September 11, 2022. The copyright holder for this preprint (which was not certified by peer review) is the author/funder, who has granted bioRxiv a license to display the preprint in perpetuity. It is made available under aCC-BY-NC 4.0 International license.

(3 and 5), the accuracy became reduced. Together with Fig. 6A, we think that the numbers of landmarks should be ≥ 7, and that 27 sets of initial values of the three rotation angles are sufficient for most of samples.

Discussion

In the present study, we developed a landmark-based 3D registration tool with subsequent 3D image reconstruction, and demonstrated that this tool worked well for the mouse blastocysts composed of several tens of nuclei. This tool contains several ways of visualizing and quantifying the registration outcomes, which enables us to objectively judge which nucleus in one image corresponds to a nucleus in another image. Importantly, for versatility in the field of experimental biology, this tool can run as ImageJ's macros.

Applicability to objects other than nucleus

We chose nuclei as landmarks, but any objects are permitted. A sole requirement of our tool is that users can identify the same position between the 1st and 2nd images. Therefore, even in the case that different markers are used between the two images, we can perform 3D registration if landmarks are correctly defined. Similarly, objects of interest (Fig. 3, step-2) are not limited to nuclei. In addition, even if we do not choose any objects of

bioRxiv preprint doi: https://doi.org/10.1101/2022.09.11.507445; this version posted September 11, 2022. The copyright holder for this preprint (which was not certified by peer review) is the author/funder, who has granted bioRxiv a license to display the preprint in perpetuity. It is made available under aCC-BY-NC 4.0 International license.

interest, we can carry out 3D image reconstruction using landmarks. These flexibilities of our tool expand the range of the applicability.

Comparison with other possible methods

Here we discuss the comparison of our method with other 3D registration methods. Except for the methods described in the Introduction section, other possible method is as follows. The most straightforward strategy of 3D registration is based on pixel-by-pixel correlation of intensities between two images. By translating and rotating one of the two images, we can search for the image transformation which gives the highest correlation. In order that this method works well, there would be some requirements. For instance, decay of intensities along Z-depth should be slight, because the decay significantly affects the value of the correlation. However, in real images of biological specimen, intensities are usually decayed along the Z-depth. Another requirement is related to image qualities, but we cannot expect comparable qualities between images from live specimen and from fixed specimen. A more critical point is its limited applicability to the cases that two specimens are stained by different markers showing different localizations: nucleus vs cytoplasm, something fluorescently labeled vs micro-CT, etc. In these cases, the correlation of intensities between the two images is meaningless. From the viewpoint of

bioRxiv preprint doi: https://doi.org/10.1101/2022.09.11.507445; this version posted September 11, 2022. The copyright holder for this preprint (which was not certified by peer review) is the author/funder, who has granted bioRxiv a license to display the preprint in perpetuity. It is made available under aCC-BY-NC 4.0 International license.

269 computational load, the search for the highest correlation in 3D translation and rotation
270 may result in unrealistic running time. By contrast, our method is based on the manual
271 choice of landmarks. Although this strategy is primitive, we can potentially label correct
272 landmarks under the above situations by considering information of tissue geometries,
273 etc. Therefore, we think that the manual choice of landmarks expands the applicability of
274 our method.

275

276 *Expertise required to implement the method*

277 Our method was developed as ImageJ/Fiji's macros (Note that we recommend Fiji but
278 not ImageJ.). For computers where Fiji is installed, the macros can run immediately after
279 downloading them (i.e. no additional setting). Usual laptops are sufficient to run the
280 macros (e.g. MacBook Air). We provide the protocols with the macros as supplementary
281 materials.

282

283

284 Appendix

285 *Definition of 3D rotation*

286 In the case of 2-dimensional situations, the rotation is defined as the following matrix;

287 $\begin{pmatrix} x_i' \\ y_i' \end{pmatrix} = \begin{pmatrix} \cos\theta & -\sin\theta \\ \sin\theta & \cos\theta \end{pmatrix} \begin{pmatrix} x_i \\ y_i \end{pmatrix}$, where θ is the rotation angle, x and y are the original

bioRxiv preprint doi: https://doi.org/10.1101/2022.09.11.507445; this version posted September 11, 2022. The copyright holder for this preprint (which was not certified by peer review) is the author/funder, who has granted bioRxiv a license to display the preprint in perpetuity. It is made available under aCC-BY-NC 4.0 International license.

coordinates, *x'* and *y'* are the coordinates after rotation, and *i* is the position of *i*th object such as nuclei and pixels. In the case of 3-dimensional situations, the rotation matrix is defined as follows;

$$\begin{pmatrix} x_i' \\ y_i' \\ z_i' \\ 1 \end{pmatrix} = \begin{pmatrix} \cos\phi\cos\theta & \cos\phi\sin\theta\sin\psi - \sin\phi\cos\psi & \cos\phi\sin\theta\cos\psi + \sin\phi\sin\psi & 0 \\ \sin\phi\cos\theta & \sin\phi\sin\theta\sin\psi + \cos\phi\cos\psi & \sin\phi\sin\theta\cos\psi - \cos\phi\sin\psi & 0 \\ -\sin\theta & \cos\theta\sin\psi & \cos\theta\cos\psi & 0 \\ 0 & 0 & 0 & 1 \end{pmatrix} \begin{pmatrix} x_i \\ y_i \\ z_i \\ 1 \end{pmatrix}$$

, where ϕ, θ, and ψ are the angles expressing the three-dimensional rotations.

Cost function to be minimized

To fit the xyz-coordinates of landmarks from a 2nd image to those from a 1st image by 3D rotation, we considered the summation of the distances between paired landmarks from the two images as follows; $G = \sum_{i=1}^{I} \left\{ \left(x_i' - X_i \right)^2 + \left(y_i' - Y_i \right)^2 + \left(z_i' - Z_i \right)^2 \right\}$, where G is the summation, I is the total number of the landmarks, and X, Y, and Z are the xyz-coordinates of the landmarks from the 1st image. We searched for the values of ϕ, θ, and ψ which minimized the value of G, and thus, G is the cost function to be minimized.

Minimization procedure

The minimization of G was achieved using a Monte Carlo algorithm. Initially, ϕ, θ, and ψ were set to be certain values: in the case of Fig. 6 where 27 sets of initial values were provided, the values of each angle were 0, (2/3) π, or (4/3) π. These values were iteratively

bioRxiv preprint doi: https://doi.org/10.1101/2022.09.11.507445; this version posted September 11, 2022. The copyright holder for this preprint (which was not certified by peer review) is the author/funder, who has granted bioRxiv a license to display the preprint in perpetuity. It is made available under aCC-BY-NC 4.0 International license.

306 modified so that the value of G became smaller, and consequently, G is expected to be
307 minimized (i.e. reaches the global minimum) unless the process is trapped at local minima.
308 The minimization procedure was implemented as a macro of ImageJ
309 (Macro_3D_particle_registration_06_v2.ijm).
310
311 *3D depiction of landmarks and objects of interest*
312 According to the xyz-coordinated of landmarks and objects of interest, they were depicted
313 as particles in 3D image (i.e. multiple Z-slices) (Fig. 4). This was implemented as a macro
314 of ImageJ (Macro_particle_drawing_02.ijm). The radius of the particles can be set by
315 users.
316
317 *3D image reconstruction*
318 When we reconstructed 3D rotated image, we applied the values of the three angles to the
319 xyz-coordinates of each pixel/voxel. The intensities of the rotated voxels are averaged by
320 a mean filter of $3 \times 3 \times 3$ kernel. This was implemented as a macro of ImageJ
321 (Macro_3D_image_rotation_02.ijm).
322
323 References

bioRxiv preprint doi: https://doi.org/10.1101/2022.09.11.507445; this version posted September 11, 2022. The copyright holder for this preprint (which was not certified by peer review) is the author/funder, who has granted bioRxiv a license to display the preprint in perpetuity. It is made available under aCC-BY-NC 4.0 International license.

Azuma, Y., and Onami, S. (2017). Biologically constrained optimization based cell membrane segmentation in C . elegans embryos. BMC Bioinformatics *18*, 307.

Bao, Z., Murray, J.I., Boyle, T., Ooi, S.L., Sandel, M.J., and Waterston, R.H. (2006). Automated cell lineage tracing in Caenorhabditis elegans. Proc. Natl. Acad. Sci. U. S. A. *103*, 2707–2712.

Heller, D., Hoppe, A., Restrepo, S., Tapon, N., Basler, K., Mao, Y., Heller, D., Hoppe, A., Restrepo, S., Gatti, L., et al. (2016). EpiTools : An Open-Source Image Analysis Toolkit for Quantifying Epithelial Growth Dynamics Technology EpiTools : An Open-Source Image Analysis Toolkit for Quantifying Epithelial Growth Dynamics. Dev. Cell *36*, 103–116.

Koyama, H., Okumura, H., Ito, A.M., Otani, T., Nakamura, K., Kato, K., and Fujimori, T. (2022). Effective mechanical potential of cell–cell interaction explains basic structures of three-dimensional morphogenesis. BioRxiv doi: https://doi.org/10.1101/812198.

Kurotaki, Y., Hatta, K., Nakao, K., Nabeshima, Y.-I., and Fujimori, T. (2007). Blastocyst axis is specified independently of early cell lineage but aligns with the ZP shape. Science *316*, 719–723.

McDole, K., Guignard, L., Amat, F., Berger, A., Malandain, G., Royer, L.A., Turaga,

bioRxiv preprint doi: https://doi.org/10.1101/2022.09.11.507445; this version posted September 11, 2022. The copyright holder for this preprint (which was not certified by peer review) is the author/funder, who has granted bioRxiv a license to display the preprint in perpetuity. It is made available under aCC-BY-NC 4.0 International license.

S.C., Branson, K., and Keller, P.J. (2018). In Toto Imaging and Reconstruction of Post-Implantation Mouse Development at the Single-Cell Level. Cell *175*, 859-876.e33.

Onuma, T.A., Hayashi, M., Gyoja, F., Kishi, K., Wang, K., and Nishida, H. (2020). A chordate species lacking Nodal utilizes calcium oscillation and Bmp for left–right patterning. Proc. Natl. Acad. Sci. U. S. A. *117*, 4188–4198.

Pokrass, M.J., and Regot, S. (2021). 3D time-lapse microscopy paired with endpoint lineage analysis in mouse blastocysts. STAR Protoc. *2*, 100446.

Pokrass, M.J., Ryan, K.A., Xin, T., Pielstick, B., Timp, W., Greco, V., and Regot, S. (2020). Cell-Cycle-Dependent ERK Signaling Dynamics Direct Fate Specification in the Mammalian Preimplantation Embryo. Dev. Cell *55*, 328-340.e5.

Preibisch, S., Saalfeld, S., Schindelin, J., and Tomancak, P. (2010). Software for bead-based registration of selective plane illumination microscopy data. Nat. Methods *7*, 418–419.

Simon, C.S., Rahman, S., Raina, D., Schröter, C., and Hadjantonakis, A.K. (2020). Live Visualization of ERK Activity in the Mouse Blastocyst Reveals Lineage-Specific Signaling Dynamics. Dev. Cell *55*, 341-353.e5.

Tan, S.E., Tan, W., Fisher, K.H., and Strutt, D. (2021). QuantifyPolarity, a new tool-kit for measuring planar polarized protein distributions and cell properties in developing

bioRxiv preprint doi: https://doi.org/10.1101/2022.09.11.507445; this version posted September 11, 2022. The copyright holder for this preprint (which was not certified by peer review) is the author/funder, who has granted bioRxiv a license to display the preprint in perpetuity. It is made available under aCC-BY-NC 4.0 International license.

tissues. Dev. *148*, dev198952. doi:10.1242/dev.198952.

Figure legends

Figure 1: Illustration of rotation and distortion of specimen during preparation

A. A tissue is illustrated with inner objects. In this case, the tissue and the inner objects are depicted as spheres.

B. An example of image acquisition of the tissue is shown. The acquired image can be shrunk or elongated along Z-axis.

C. A rotated tissue is shown. During experimental procedures including fixation, the tissue may be rotated ("a tissue axis" between B and C).

Figure 2: Rotated image of mouse blastocyst

The 1st and 2nd images are acquired from a live or fixed embryo. A Z-slice, maximum intensity projection (MIP), and 3D view of the images are shown. The regions of the inner cell mass are illustrated for each image. Landmarks and objects of interest were labeled by using ImageJ>Multi-point tool.

bioRxiv preprint doi: https://doi.org/10.1101/2022.09.11.507445; this version posted September 11, 2022. The copyright holder for this preprint (which was not certified by peer review) is the author/funder, who has granted bioRxiv a license to display the preprint in perpetuity. It is made available under aCC-BY-NC 4.0 International license.

Figure 3: Procedures of 3D registration and reconstruction

A. The procedures of our method are illustrated. At step-0, microscopic images are shown where the 2nd image is rotated compared with the 1st image. At the "Optional" step, the shrinkage or elongation of the two images is corrected (arrows). At the step-1, 4 landmarks are exemplified (#1-4). At the step-2, objects of interest are labeled by non-overlapped numbers between the two images (#5-8 vs #9-12). At the step-3, shrinkage or elongation of the xyz-coordinates of the landmarks and the objects of interest are corrected. If shrinkage or elongation of the images has been already corrected at the "Optional" step, the step-3 is not required. At the step-4, the landmarks in the 2nd image are optimally rotated. At the step-5, the paired objects are identified (e.g. 5-12, 6-11). At the step-6, the 2nd image is rotated to be aligned with the 1st image, and the rotated image is reconstructed.

B. Definition of 3D rotation is explained. In the case of 2D rotation, the rotation matrix contains one angle (θ in Appendix 1). In the case of 3D rotation, the rotation matrix contains three angles (ϕ, θ, and ψ in Appendix 1).

Figure 4: Registration of landmarks and objects of interest

A. Landmarks in the 1st and 2nd images are depicted as particles in 3D images. Images

bioRxiv preprint doi: https://doi.org/10.1101/2022.09.11.507445; this version posted September 11, 2022. The copyright holder for this preprint (which was not certified by peer review) is the author/funder, who has granted bioRxiv a license to display the preprint in perpetuity. It is made available under aCC-BY-NC 4.0 International license.

396 before and after the rotation of the 2nd image are shown. The 3D images were generated
397 by using Fiji>Plugins>3D Viewer; all 3D images in this article were generated by the 3D
398 Viewer.
399 B. Objects of interest in the 1st and 2nd images are depicted as particles in 3D images. The
400 landmarks are also depicted. Yellow circles, some examples of paired objects; light blue
401 circles with dashed lines, a few examples of unsuccessfully paired objects.
402 C. Quantitative evaluation of pairing. For each object of interest in the 1st image, three
403 objects as a candidate for pairing are shown in the 2nd image according to distances
404 between the objects. Four objects in the 1st image are exemplified. In the case that an
405 object in the 2nd image is multiply assigned as the nearest neighbor for different objects
406 in the 1st image, such multiply-assigned objects are also listed in the output text file (not
407 shown in this figure).
408 D. Paired objects between the 1st and 2nd image are depicted as particles in the same color.
409 Arrows, three examples of paired objects. Landmarks are also depicted. The original
410 images were 8-bit images where the intensities of each particle correspond to the IDs of
411 the objects, and the color was provided by setting lookup tables (ImageJ>Image>Lookup
412 Tables>3-3-2-RGB).
413

bioRxiv preprint doi: https://doi.org/10.1101/2022.09.11.507445; this version posted September 11, 2022. The copyright holder for this preprint (which was not certified by peer review) is the author/funder, who has granted bioRxiv a license to display the preprint in perpetuity. It is made available under aCC-BY-NC 4.0 International license.

Figure 5: 3D reconstruction of rotated image

A. 3D images of the 1st and the rotated 2nd image are shown for two blastocysts (#1 and #2). The 2nd images before rotation are shown in Fig. 2 for #1 or in the bottom panel for #2. Note that before the rotation, the intensities of the 2nd images were normalized along the Z-axis (ImageJ>Process>Enhance Contrast...>Normalize), and thus, the intensities were not conserved.

B. Two z-slices of the merged image of the blastocyst #1 are exemplified. Yellow, examples of paired nuclei between the 1st and the rotated 2nd images.

C. A merged image is exemplified where images of nuclei can be the 1st or the rotated 2nd images, and particles images constructed in Fig. 4 can be the 1st or the rotated 2nd images. In other words, 4 (2×2) combinations of merged images can be generated. The merged image was generated by ImageJ>Image>Color>Merge Channels…

Figure 6: Performance and accuracy of 3D registration

A. The performance of the minimization process was evaluated. The probability of successful minimization among 27 trials is shown for each blastocyst (#1-#4); the probability = 1.0 means that all 27 trials successfully reached the global minimum. For the numbers of landmarks = 9, $N = 1$. For the numbers = 3, 5, or 7, landmarks were

bioRxiv preprint doi: https://doi.org/10.1101/2022.09.11.507445; this version posted September 11, 2022. The copyright holder for this preprint (which was not certified by peer review) is the author/funder, who has granted bioRxiv a license to display the preprint in perpetuity. It is made available under aCC-BY-NC 4.0 International license.

randomly chosen from the 9 landmarks, and 4 sets of different landmarks were generated; $N = 4$.

B. Accuracy of pairing of objects was evaluated for the outcomes of the successful minimization in A. Similar to A, the 4 blastocysts were tested with different number of landmarks for each blastocyst.

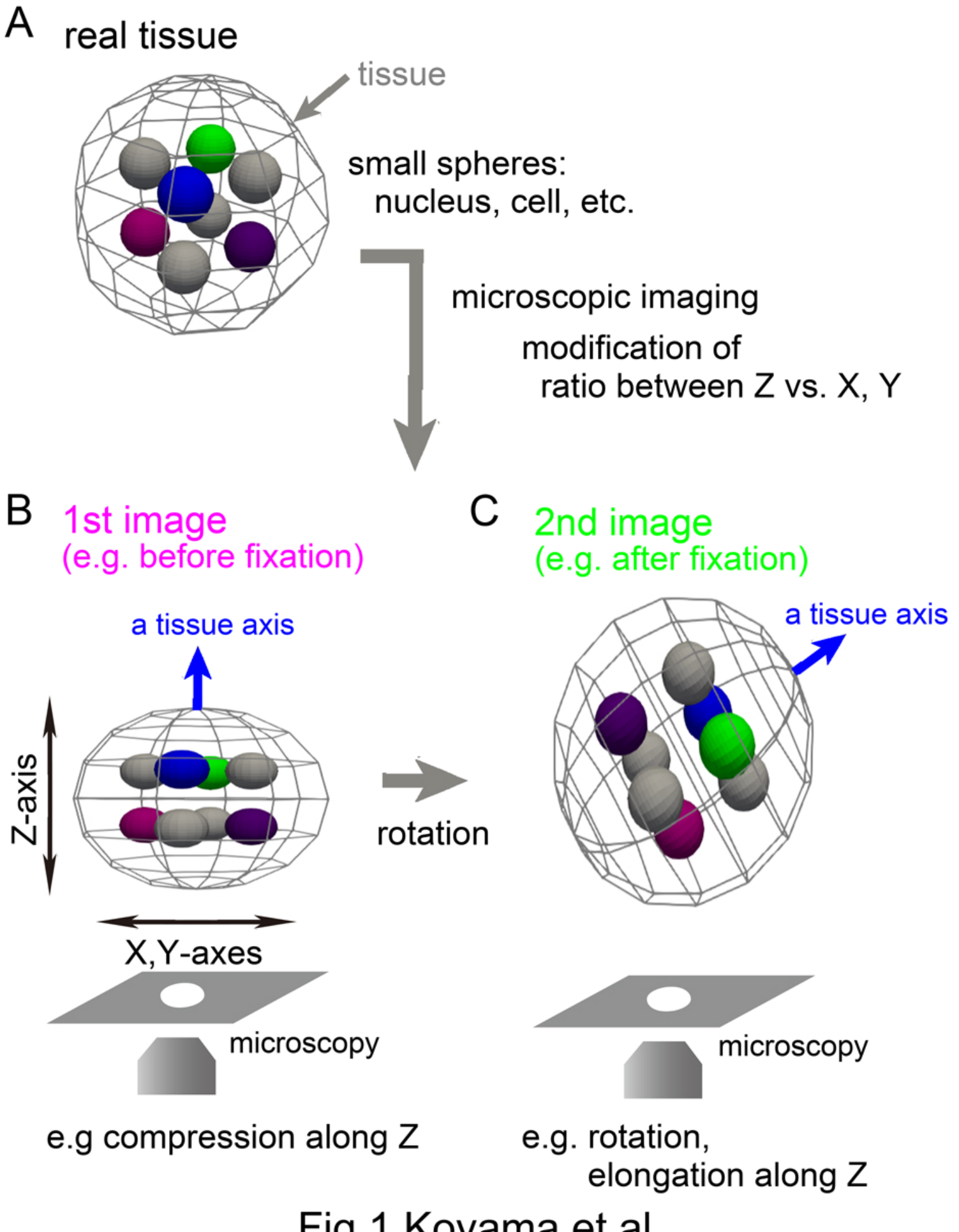

Fig.1 Koyama et al.

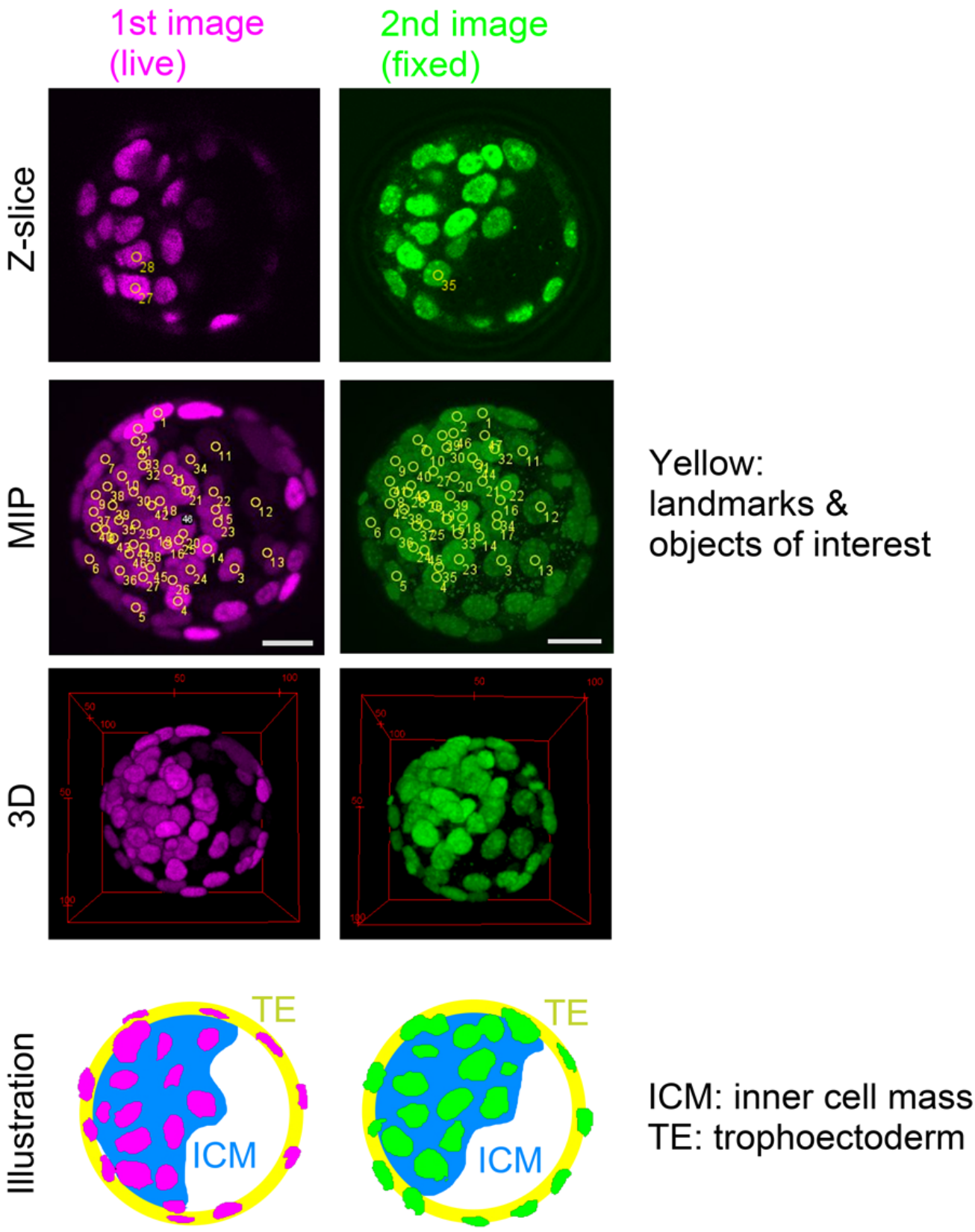

Fig.2 Koyama et al.

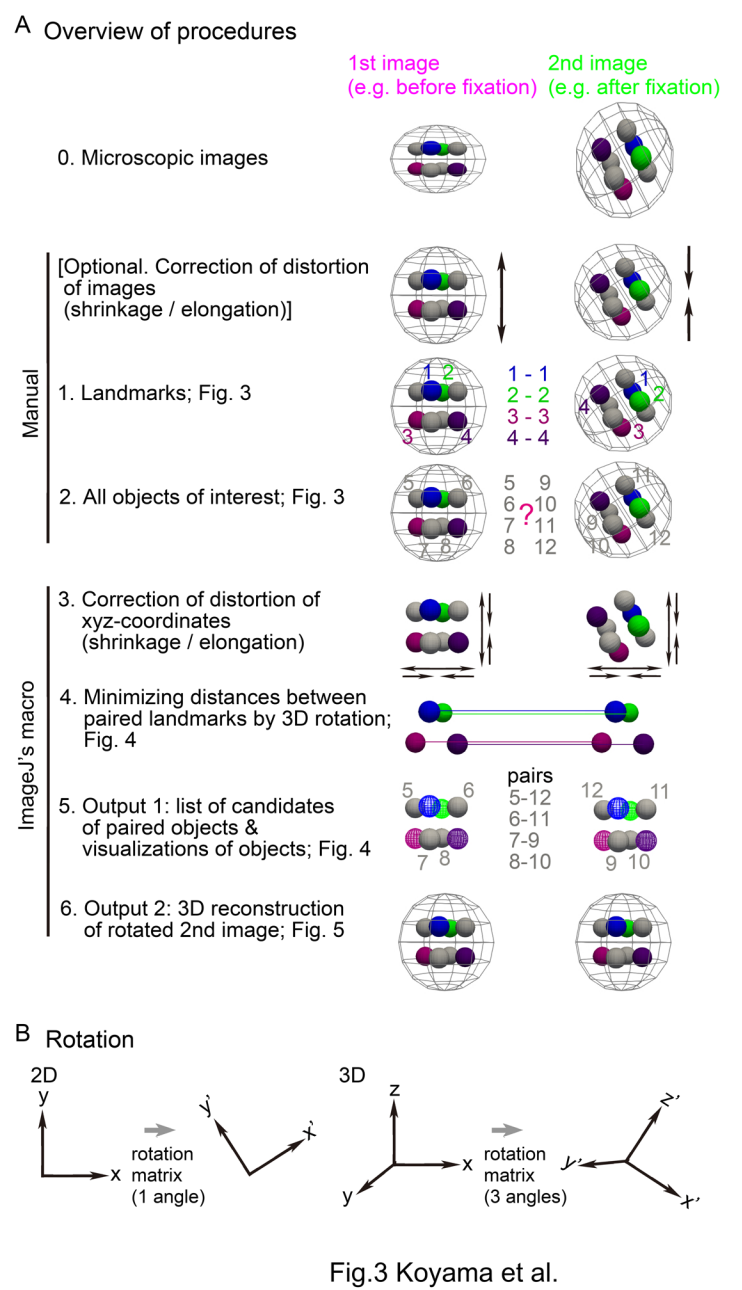

Fig.3 Koyama et al.

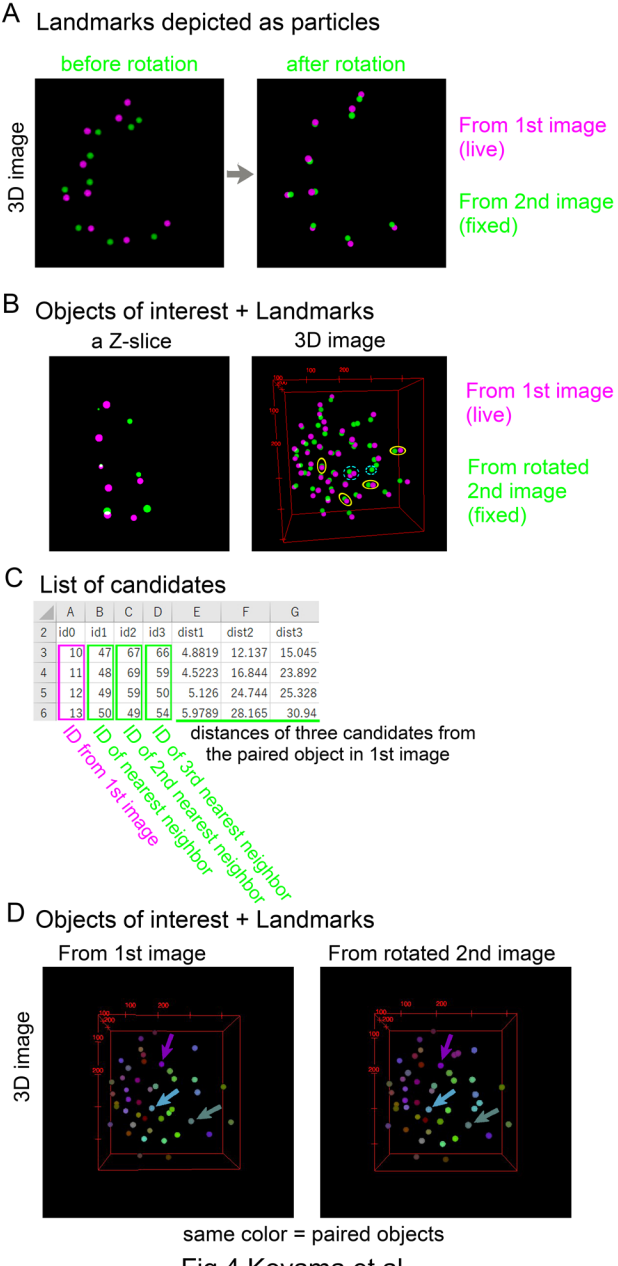

	A	B	C	D	E	F	G
2	id0	id1	id2	id3	dist1	dist2	dist3
3	10	47	67	66	4.8819	12.137	15.045
4	11	48	69	59	4.5223	16.844	23.892
5	12	49	59	50	5.126	24.744	25.328
6	13	50	49	54	5.9789	28.165	30.94

Fig.4 Koyama et al.

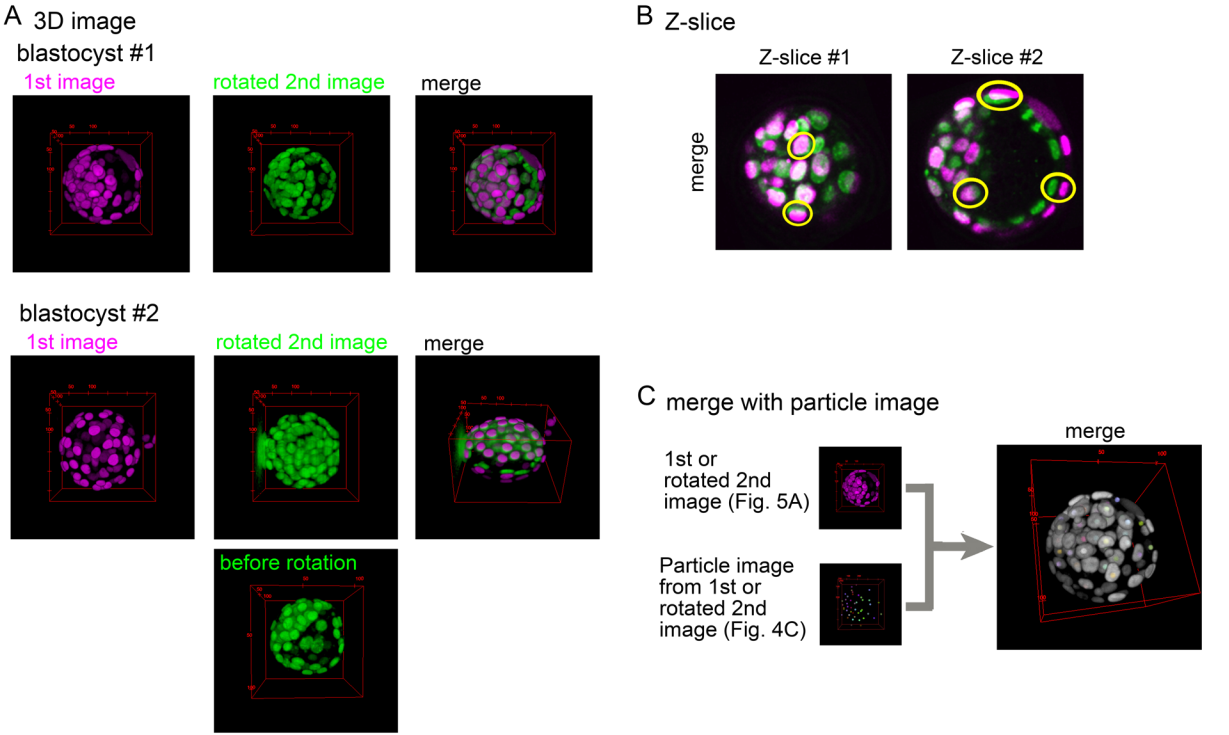

Fig.5 Koyama et al.

A Probability of successful minimization

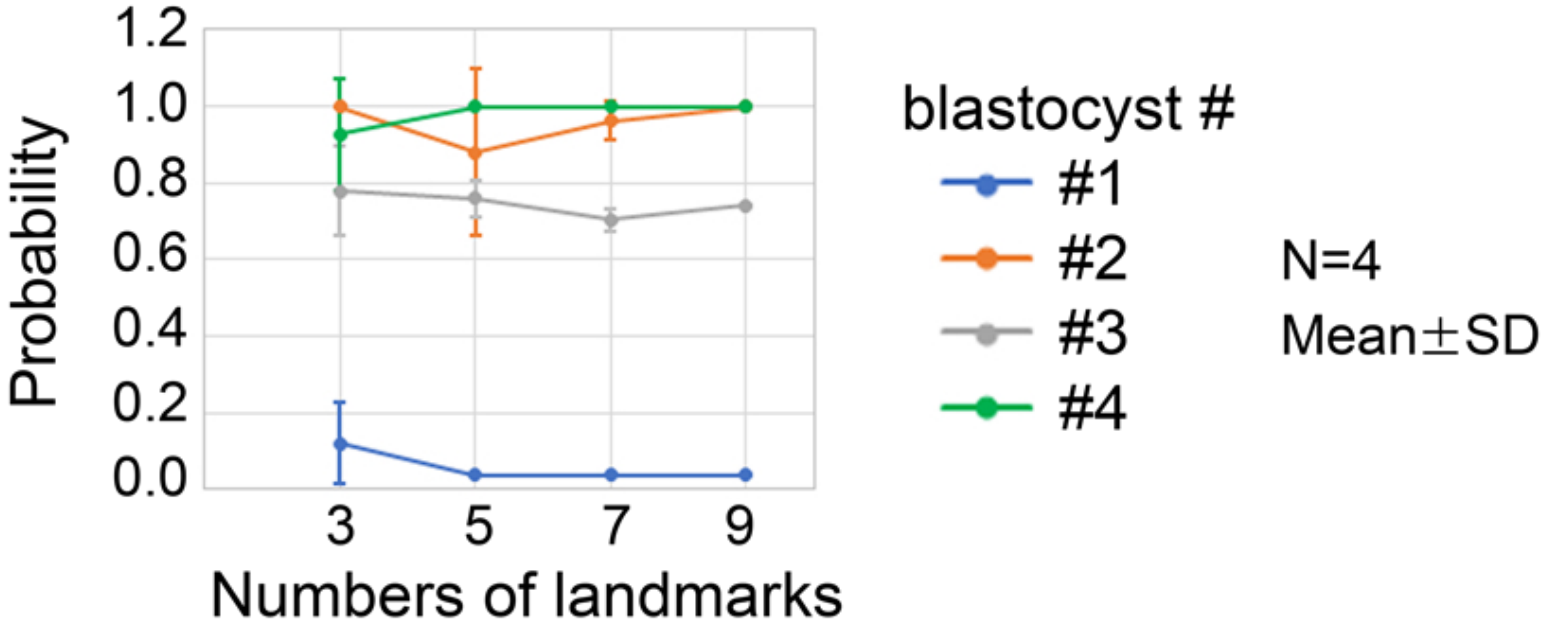

B Accuracy of pairing

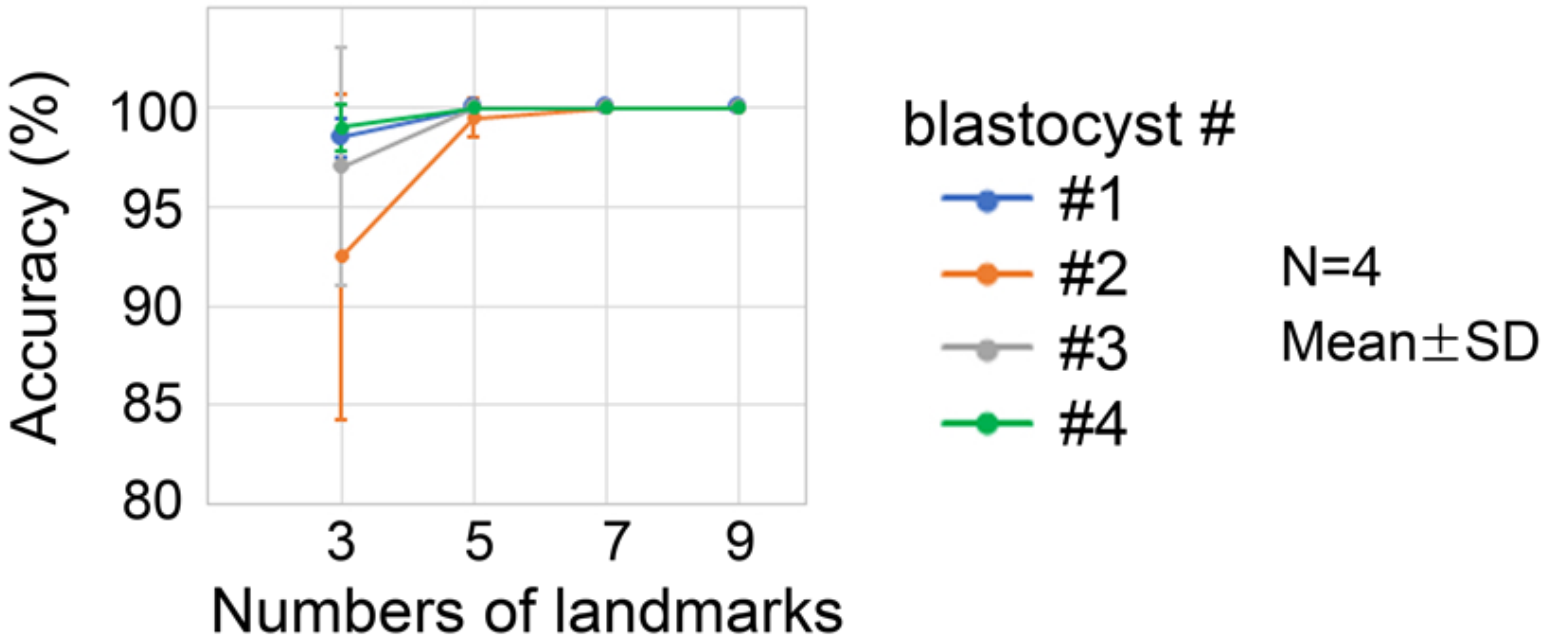

Fig.6 Koyama et al.